We are IntechOpen, the world's leading publisher of Open Access books
Built by scientists, for scientists

5,300
Open access books available

130,000
International authors and editors

155M
Downloads

154
Countries delivered to

Our authors are among the

TOP 1%
most cited scientists

12.2%
Contributors from top 500 universities

CLARIVATE ANALYTICS

BOOK CITATION INDEX

INDEXED

WEB OF SCIENCE™

Selection of our books indexed in the Book Citation Index
in Web of Science™ Core Collection (BKCI)

Interested in publishing with us?
Contact book.department@intechopen.com

Numbers displayed above are based on latest data collected.
For more information visit www.intechopen.com

Chapter

Microwave Imaging for Breast Cancer Detection

Yoshihiko Kuwahara

Abstract

Microwave imaging (MI) is characterized by no exposure, stronger contrast between soft tissues than X-rays and ultrasound, and a smaller device scale. This chapter describes the electrical properties of the breast tissue that underlie MI, and then outlines the MI hardware configuration and three imaging algorithms: confocal imaging, scattering tomography, and near-field holography. After that, we will introduce the actual equipment and experimental results using the three imaging algorithms. Finally, we will summarize the challenges of realizing a medical imaging device using MI.

Keywords: microwave imaging, complex permittivity, confocal imaging, scattering tomography, near-field holography

1. Introduction

Breast cancer begins in the late 20s, but the mammary glands are well developed in the 20s and 30s, making initial diagnosis by X-ray mammography, which is a general examination, difficult. There is an ultrasonic diagnostic device (US) as an alternative method, but the reliability of the diagnosis depends on the skill of the inspector, the reproducibility of the data is poor, and continuous tomographic images cannot be obtained [1]. On the other hand, magnetic resonant image (MRI) and positron emission tomography (PET) are not candidates for examination equipment because of their large scale, long examination time, and high cost. Microwave imaging (MI) has a stronger contrast between soft tissues than X-rays and ultrasound. MI is not exposed to radiation, and has the characteristics of being small in scale and inexpensive. However, there are problems to be solved and it has not yet been put into practical use.

There are two types of MI, scattering tomography (ST), which solves the inverse scattering problem and reconstructs the relative permittivity and conductivity distribution in the breast, and confocal imaging (CI), which reconstructs the scattered power distribution [2]. In principle, the former can reconstruct the shape of intramammary tissue and is suitable as a diagnostic device. However, the inverse scattering problem is a non-linear ill-posed problem with more unknowns (relative permittivity / conductivity distribution in the breast) than the number of equations (measurement data), and is susceptible to modeling, manufacturing, and measurement errors. The latter has been clinically imaged by several research groups, including the author, and strong scattering has been confirmed around the cancer [3–6]. However, even in breasts without lesions, meaningless scattered images

(artifacts) appear due to multiple reflections in the breast, so how to identify the presence or absence of cancer is an issue.

In recent years, as a third method, research on near field holographic imaging (NFHI), which can reconstruct the shape of intramammary tissue, is also in progress [7, 8]. Since the principle of image reconstruction of NFHI is based on the principle of Fourier transform, the time required for image reconstruction is short. However, there are still problems that a huge amount of observation data is required to increase the resolution and that images cannot be reconstructed correctly with high-contrast objects.

In this chapter, we first explain the electrical properties of breast tissue, which is the basis of MI, based on large-scale measurement data [9]. Next, the basic device configuration of MI, three imaging algorithms, and the features of CI, ST, and NFHI are described. Next, we will introduce the equipment that implements these algorithms and the experimental results. Finally, the issues of MI and future prospects will be described.

2. Electrical properties of breast tissue

Living tissue has different electrical properties depending on the tissue, and when electromagnetic waves are incident, reflection occurs at the boundary. The basis of MI is to detect reflections that occur at tissue boundaries. This section describes the electrical properties of breast tissue.

2.1 Complex permittivity and Debye model

Living tissue is a lossy dielectric, and when an electromagnetic wave is incident, its wavelength is shortened and propagates while being attenuated. When an electromagnetic wave having a main polarization in the x-axis direction propagates in the z-axis direction through a dielectric having a loss, the electric field at an arbitrary distance z is expressed by the following equation.

$$E_x = E_0 e^{-\alpha z} e^{-j\beta z} \tag{1}$$

Here, E_0 is the electric field at $z = 0$, α and β are the attenuation constant and the phase constant, and are expressed as follows using the relative permittivity ε_r, conductivity σ, and angular frequency $\omega = 2\pi f$ of the propagation medium.

$$\alpha = \frac{\omega}{c_0} \sqrt{\frac{\varepsilon_r}{2}} \left[\sqrt{1 + \left(\frac{\sigma}{\omega \varepsilon_0 \varepsilon_r}\right)^2} - 1 \right]^{1/2} \tag{2}$$

$$\beta = \frac{\omega}{c_0} \sqrt{\frac{\varepsilon_r}{2}} \left[\sqrt{1 + \left(\frac{\sigma}{\omega \varepsilon_0 \varepsilon_r}\right)^2} + 1 \right]^{1/2} \tag{3}$$

Here, c_0 is the speed of light propagating in the vacuum, and ε_0 is the permittivity of the vacuum.

The dielectric material with loss is represented by the complex permittivity.

$$\varepsilon(\omega) = \varepsilon_r \varepsilon_0 + \frac{\sigma}{j\omega} \tag{4}$$

It can be seen that the imaginary part of the complex permittivity changes with frequency. By the way, it is known that the real part of the complex permittivity of a living body changes depending on the frequency. The property of such a material is called dispersibility. The complex relative permittivity of dispersible materials can be modeled by the following equation [10].

$$\frac{\varepsilon(\omega)}{\varepsilon_0} = \varepsilon_\infty + \frac{\sigma_s}{j\omega\varepsilon_0} + \frac{\Delta\varepsilon}{1+j\omega\tau} \tag{5}$$

The curve of the complex relative permittivity represented by Eq. (5) is called the Debye model. **Figure 1** shows the result of measuring the complex relative permittivity of the mammary gland tissue by the probe method [11] (solid line) and the approximate curve (dotted line) modeled by Eq. (5). Here, ε_∞, $\Delta\varepsilon$, σ_s, and τ are estimated by the simplex method [12] so that the squared norm of the difference between the measured value and the frequency characteristic of the complex permittivity expressed in Eq. (5) is minimized. When the respective values are -1.22, 59.1, 0.92, 10.4 ps, the frequency characteristics of the measurement and the Debye model are almost the same. Since wideband electromagnetic waves are often used in confocal imaging, it is desirable to model objects using ε_∞, $\Delta\varepsilon$, σ_s, and τ when performing propagation analysis.

2.2 Complex permittivity measuring device

The electrical constants of breast tissue can be measured using a dielectric probe [9, 11]. Ref. [11] shows that a cylindrical region with a depth of 1.5 mm and a radius of 3.75 mm is required to achieve a measurement error of 10% using a 2.2 mm diameter dielectric probe. In our study, we measure the complex permittivity of breast tissue
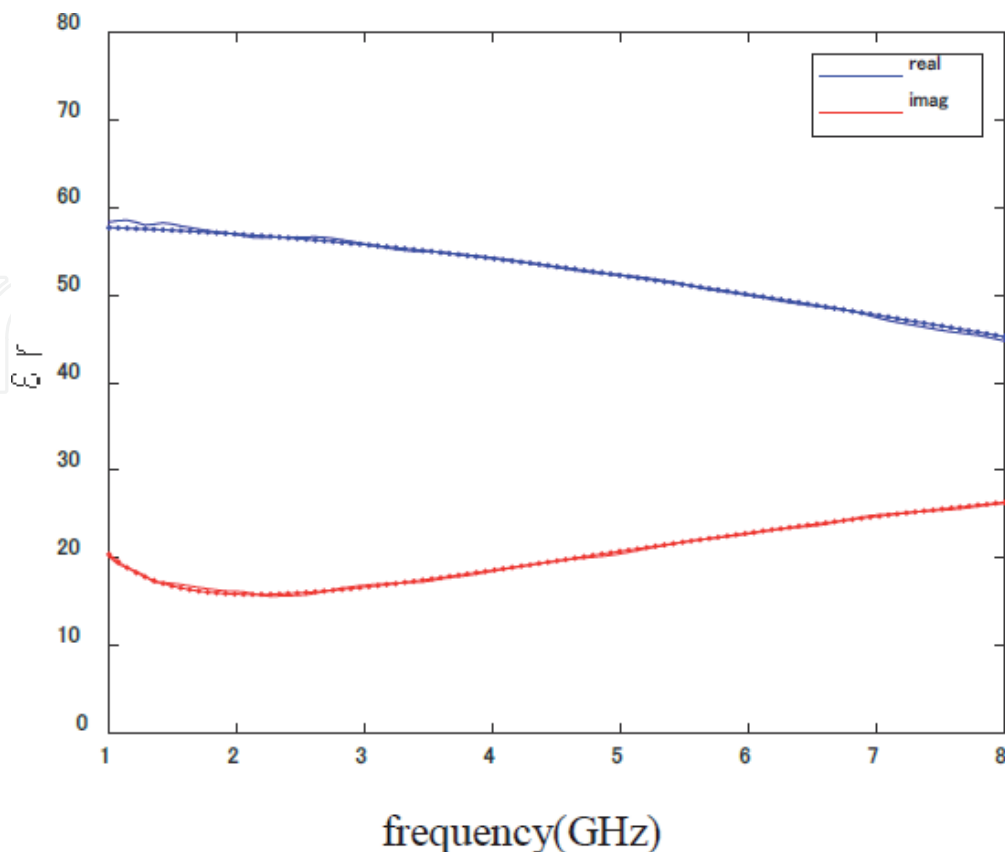

Figure 1.
Complex dielectric constant of glandular tissue and approximation by Debye model.

using a 2.2 mm diameter dielectric probe in the dielectric measurement kit Keysight 85070E and a vector network analyzer, E5071C. The measurement range is 1–8 GHz.

In recent year, since breast cancer is often detected at an early stage, the size of the tumors removed by surgery has become smaller. To investigate the minimum required volume of a specimen, the dielectric constant was measured by placing ketchup in containers of various volumes. Ketchup is readily available and has about the same electrical constant as cancer. The container, apart from the petri dish, was created using a 3D printer. The material of the container is ABS resin. **Figure 2** illustrates the appearance of the container and measurement system.

In the preliminary measurement using ketchup, for a container measuring 0.5 × 0.5 × 0.5 cm, an error of 3% occurred with respect to the measurement result of the petri dish. However, in a container measuring 1 × 1 × 0.5 cm, the error reduces to 1% or lower. We selected the 1 × 1 × 0.5 cm container for analysis. Samples removed by surgery were cut into fats, mammary glands, and cancerous tumor tissues. Each tissue was placed in a container and the probe was pressed downwards to measure the complex permittivity. **Figure 3** shows a photograph of the tissue put in a container.

2.3 Measurement

2.3.1 Population of measurements

During the breast cancer surgery performed at Aichi Medical University from May 2018 to July 2020, breast tissue specimens were collected from 140 patients who consented to the specimen collection [9]. **Table 1** shows the number of samples and the average age of the patients classified by case. Here, mammary gland tissues of the highest possible density were collected from every patient.

In recent years, there have been many stage 0 and stage 1 (tumors less than 2 cm) surgery, and it has not been possible to collect tumor tissues that can withstand measurement from all patients. X-ray mammography findings of mammary gland density revealed that nearly half of the patients had dense mammary glands. Due to the disappearance of mammary gland tissue at an older age, it was not possible to obtain mammary gland tissue that could be used for measurement from all patients.

Invasive ductal carcinoma accounts for 84%, of which more than half are scirrhous type. Fibroadenoma is more common in young women, with a minimum age of onset of 15 in this study. Five patients in their 30s with invasive ductal carcinoma account for 4% of all patients with invasive ductal carcinoma. All of the patients were at stage 2. Women in their 30s are not eligible for breast cancer screening in Japan. When cancer grows, it is said that necrosis and calcification occur in the center of the cancer. X-ray mammography detects this calcification. In the pathological findings, there were necrosis in 6 cases and calcification in 11 cases.
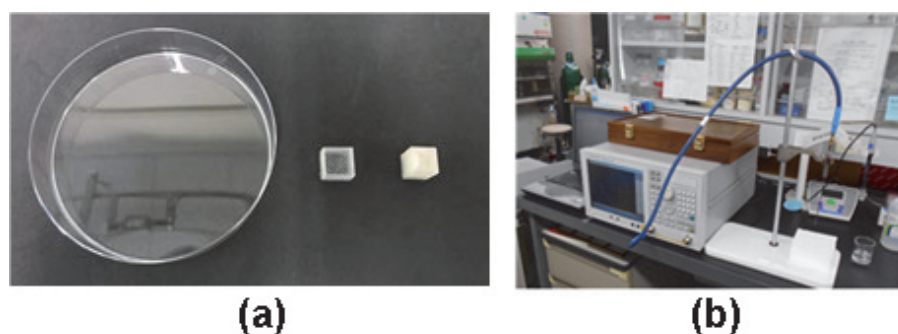

(a)   **(b)**

Figure 2
(a) Containers of various volumes, petri dish 1×1×0.5 cm, 0.5×0.5×0.5 cm container. (b) Measurement equipment for complex permittivity.
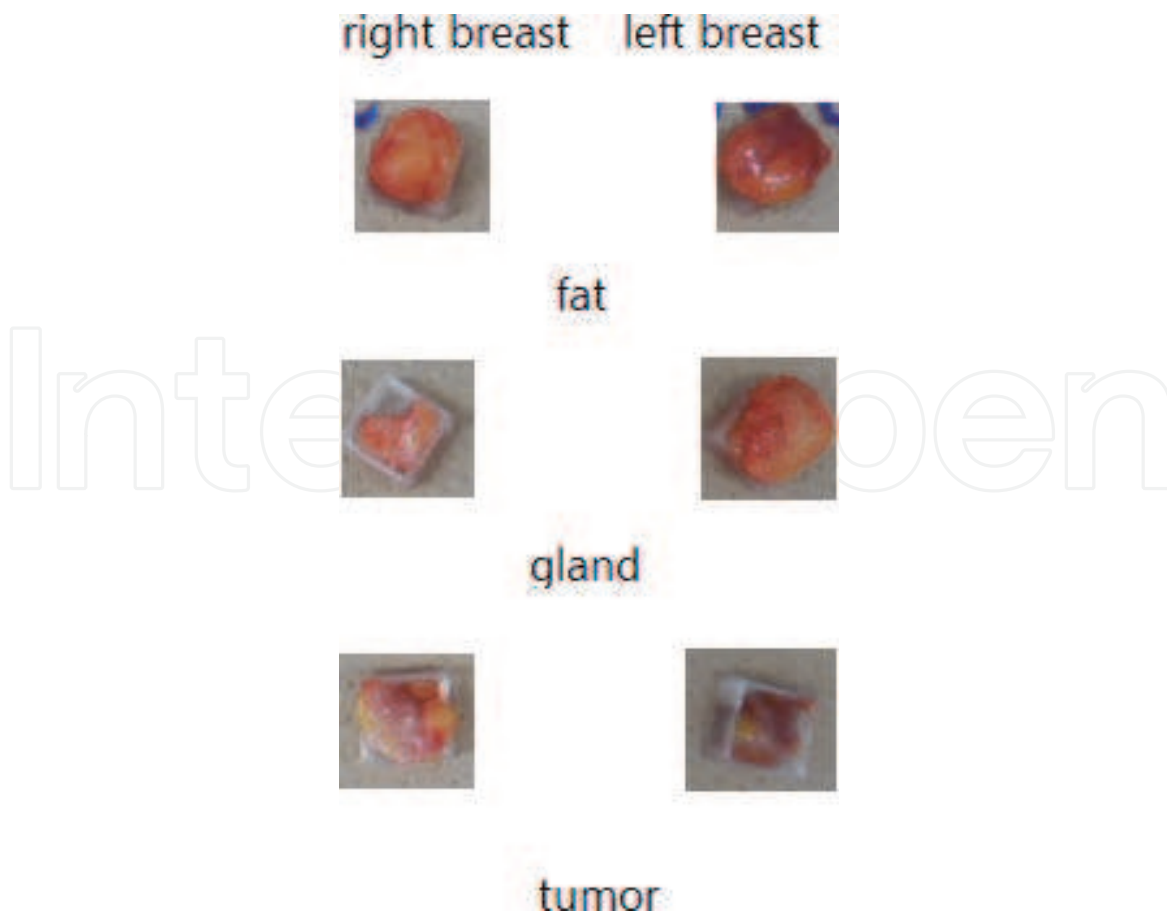
Figure 3.
Tissue samples.

Histological classification		Patient	Tumor	Gland	Fat	Age (years)
Invasive ductal carcinoma	Tuble forming	7	6	6	6	59.6
	Solid	38	35	23	36	63.3
	Scirrhous	64	52	46	58	61
	Others	9	8	6	9	59.9
Special	Invasive lobular carcinoma	4	4	4	4	63.6
	Mucinous carcinoma	6	6	4	5	66.8
	Others	5	0	5	5	49.4
Mixed connective tissue and epithelial tumors	Fibroadenoma	5	5	4	2	31.1
	Phyllodes tumor	2	2	0	1	54.2
Total		140	118	98	126	60.3

Table 1.
Number of samples taken out by surgery.

2.3.2 Measurement results

Figure 4 shows a typical example of the complex relative permittivity of the sample measured using the measurement system shown in **Figure 2**. The measurement result that we expect is that the relative permittivity of tumor tissue is considerably higher than that of mammary tissue, as shown in **Figure 4a**. However,
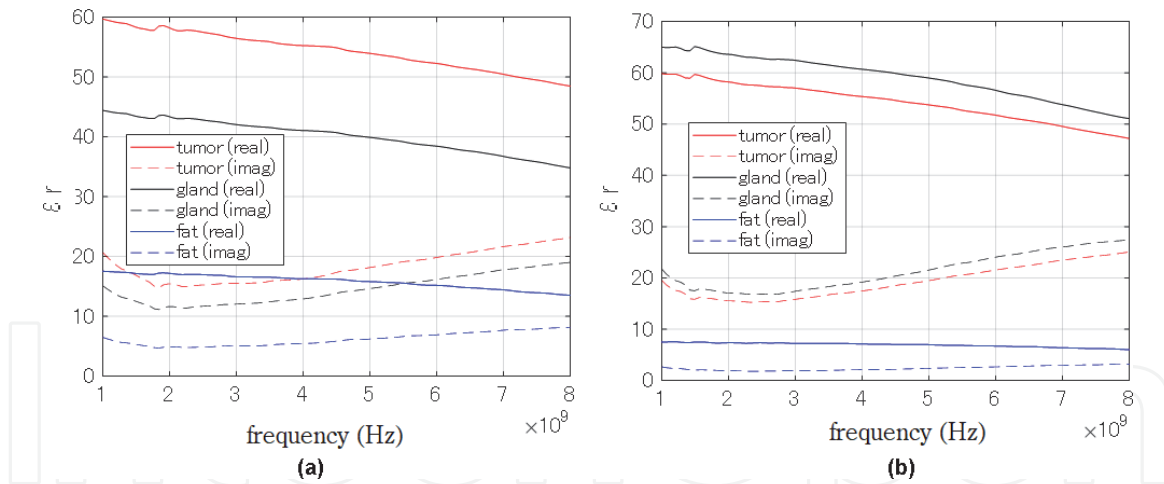
Figure 4.
(a) Measurement example of the complex permittivity, solid tubular carcinoma (Age 49, dense breast). (b) Measurement example of the complex permittivity, Scirrhous carcinoma (Age 49, dense breast).

as shown in **Figure 4b**, there were 8 cases in the scirrhous type and 1 case in the solid type in which the relative permittivity of the mammary gland tissue was higher than that of the tumor tissue. The reason for the opposite properties may be that, as noted in the Ref. [13], not all areas of the tumor sample are filled with tumor tissue.

Table 2 shows the average of relative permittivity ε_r and conductivity σ of tumor and mammary gland at 1.6 GHz by pathology. On average, the relative permittivity of cancer is 17.5% higher than that of mammary gland tissue, and the conductivity is 16.2% higher.

Fibroadenoma has the lowest contrast between the relative permittivity and conductivity of cancer and mammary gland. Fibroadenoma is common in women in their teens and 20s, has well-defined lump boundaries, and is often classified as a benign tumor. The disease is not a tumor, but is made up of an excessive amount of normal cells (anaplasia), so there is almost no difference in contrast with the mammary gland. Among the invasive cancers, tumors that are said to be a special type have a large contrast between the mammary gland and the cancer, and good

Histological classification		Tumor		Mammary gland	
		ε_r	σ [S/m]	ε_r	σ [S/m]
Invasive ductal carcinoma	Tuble forming	60.5	1.66	50.1	1.4
	Solid	58.6	1.59	49.8	1.39
	Scirrhous	58.9	1.65	52.4	1.47
	Others	59.6	1.63	41.6	1.15
Special	Invasive lobular carcinoma	58.4	1.63	43.0	1.19
	Mucinous carcinoma	65.3	1.93	45.9	1.3
	Others	—	—	53.4	1.5
Mixed connective tissue and epithelial tumors	Fibroadenoma	62.7	1.74	60.2	1.73
	Phyllodes tumor	61.7	1.61	—	—
Total		59.5	1.65	50.6	1.45

Table 2.
Averaged permittivity and conductivity.

detection by microwave imaging can be expected. The scirrhous type is the most common type of invasive ductal carcinoma, but the contrast between the relative permittivity and the conductivity of the cancer and mammary gland tissue is 12%, which is relatively small. Therefore, MI requires the ability to identify objects with a contrast of about 10%.

Table 3 shows the average Debye parameters for tumor and mammary gland by pathology. The Debye parameter is a parameter considering dispersibility (frequency characteristic). Relaxation time τ does not differ significantly between

| Histological classification		Tumor				Mammary gland			
		ε_∞	$\Delta\varepsilon$	σ_s	τ [ps]	ε_∞	$\Delta\varepsilon$	σ_s	τ [ps]
Invasive ductal carcinoma	Tuble forming	5.63	55.9	0.94	11.6	1.25	49.7	0.77	11.5
	Solid	3.91	55.5	0.90	11.2	1.56	49.0	0.81	10.7
	Scirrhous	4.59	55.2	0.95	11.4	0.59	52.5	0.85	10.5
	Others	3.39	57.0	0.97	10.3	1.81	40.4	0.64	10.3
Special	Invasive lobular carcinoma	5.28	53.9	0.97	11.0	−0.45	44.0	0.70	9.9
	Mucinous carcinoma	−1.76	66.2	0.98	10.3	−4.71	47.0	0.68	9.8
	Others	—	—	—	—	−1.88	55.9	0.90	9.7
Mixed connective tissue and epithelial tumors	Fibroadenoma	1.46	61.8	0.96	11.1	1.99	56.3	0.96	11.8
	Phyllodes tumor	−0.45	63.0	0.89	10.3	—	—	—	—
total		3.87	56.3	0.94	11.2	0.64	50.5	0.81	10.6

Table 3.
Debye parameters.
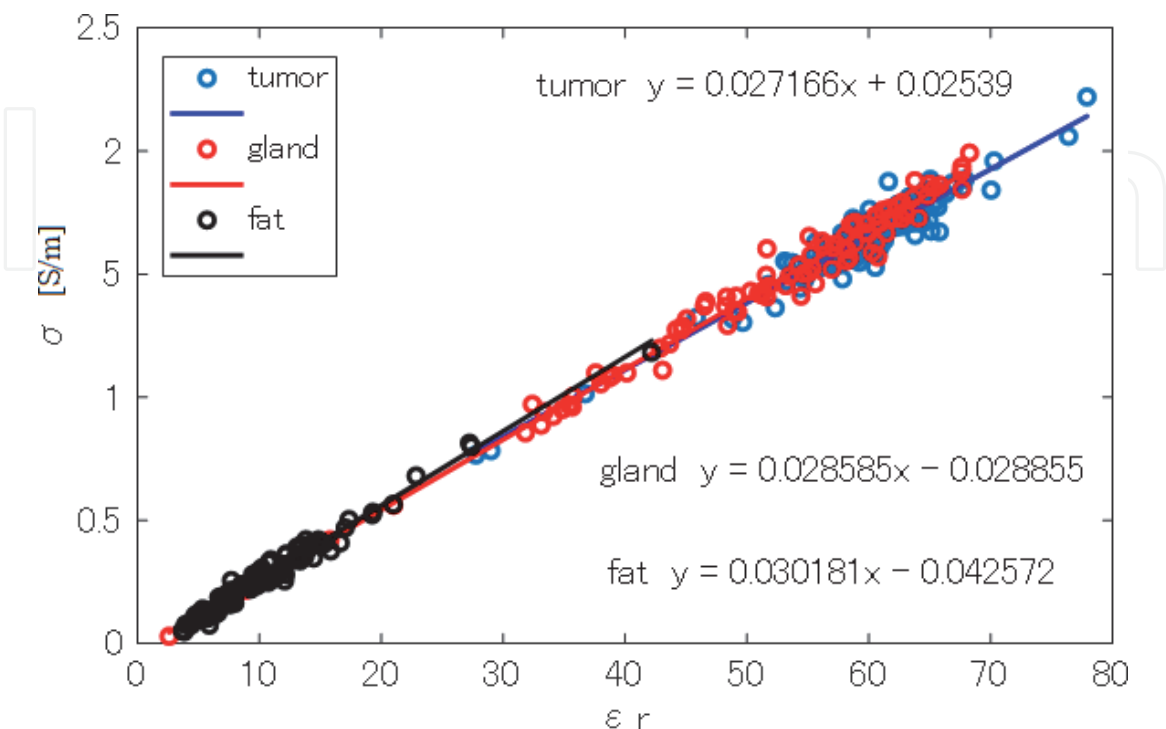
Figure 5.
Linear relationship between relative permittivity and conductivity.

tumor tissue and mammary gland tissue. This is an important prior knowledge of ST for solving the inverse scattering problem [14]. Among the Debye parameters, ε_∞ has an extremely high contrast between cancer and mammary gland. By utilizing this feature, it will become easy to distinguish between the mammary gland and cancer in microwave imaging.

Figure 5 is a plot showing the relationship between relative permittivity ε_r and conductivity σ of breast tissue at 1.6 GHz, It shows that there is a strong correlation between ε_r and σ. This is also important priori information for ST to solve the inverse scattering problem [15].

3. Microwave imaging

This chapter gives an overview of the configuration of an imaging device using microwaves and the algorithm for reconstructing images. The details of the reconstruction algorithm are omitted due to space limitations. For details of the reconstruction algorithm, refer to the related literature.

3.1 Equipment configuration

Figure 6 shows the hardware configuration of the MI system. Multiple antennas are placed around the object. One antenna is selected to transmit electromagnetic waves, and all antennas including the antenna used for transmission receive and record scattered waves from the imaging target. The observation data group X_{nn} (n = 1, .., N) is collected by changing the antenna used for transmission one after another. The first digit of the subscript of X_{nn} indicates the transmission condition number, and the second digit indicates the reception condition number. When transmitting and receiving using 18 antennas, N = 18 and $18 \times 18 = 324$ observation data groups can be obtained. If multiple signals are received at the same time, the hardware configuration becomes complicated, so a changeover switch is used for time-division reception. A commercially available vector network analyzer (VNA) can be used as the transmitter / receiver. Since short pulses are equivalent to wideband frequency sweep signals, VNA can be used even with radars that use pulses.

3.2 Imaging algorithm
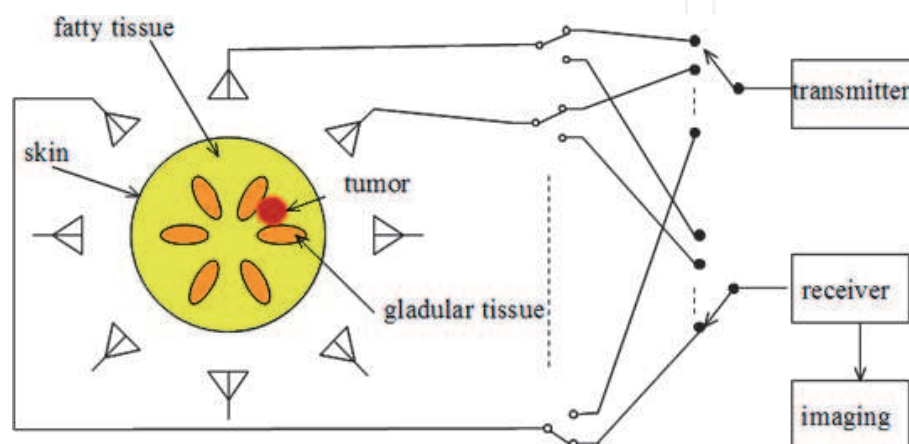
Table 4 shows typical image reconstruction methods.

Figure 6.
Hardware of the MI system.

	CI	NFHI	MT
Reconstructed Image	Scattered power distribution	Reflection coefficients distribution	Complex permittivity distribution
Reproduction of tissue shape	Impossible	Possible	Possible
Processing time	Short	Very short	Long
Installation	Easy	difficult	difficult
Problems	• Identification of abnormal tissue	• Means for acquiring a large amount of observation data. • Investigating the effects of multiple reflections between objects	• Accuracy / resolution • Establishment of calibration method. • Design of high sensitivity antenna
Reference	[3–6, 16–19]	[7, 8, 20]	[14, 15, 21–25, 28]

Table 4.
Image reconstruction method.

The principle of image reconstruction of CI is the same as that of ultrasonic diagnostic equipment. That is, while shifting the focal point set in the imaging region, the magnitude of the scattered wave at the focal point is calculated and the magnitude distribution is visualized. Electromagnetic waves are more attenuated in the body than ultrasonic waves, and objects embedded in the high contrast tissue cannot accurately reproduce the tissue image due to the multiple reflections. Reconstructed images of breasts of breast cancer patients have been reported by the author and several other research institutes [3–6]. In all reports, large reflection images were observed around the cancer, but the shape and size of the cancer could not be accurately reconstructed. In addition, meaningless images are reconstructed even in cancer-free breasts. Doctors make a diagnosis from the reconstructed image, but it is not possible to make an accurate diagnosis because the tissue shape is not accurately reconstructed.

NFHI reconstructs the reflection coefficients' distribution in the imaging region, and the reconstructed image reflects the shape of the tissue [20]. Since the image reconstruction is based on the Fourier transform of the spatial region, the reconstruction time is extremely short and real-time display will be possible. The problem is that the resolution is governed by the sampling theorem, so a huge amount of observation data is required to obtain a high-definition reconstructed image, and it is difficult to realize a practical data acquisition system. For example, in order to obtain a spatial resolution of 2 mm, observation data for each 2 mm is required on the projection surface of the imaging region, and observation data at 2500 positions is required assuming an observation surface of 100 mm × 100 mm. Data can be acquired by mechanical scanning of the antenna, but the observation time will be significantly longer. If the antenna is an array to save time, 2500 transmitters and receivers are required, which increases the cost and limits the aperture length of one antenna to 2 mm or less. In this case, millimeter waves should be used, but the attenuation is extremely large in the body, which is not practical. Another issue is that the currently proposed 3D reconstruction algorithm does not take into account the effects of multiple reflections within the imaging region, making reconstructed images of object with a large size or a complicated structure difficult.

Research by the authors has shown that NFMI can, in principle, reconstruct the tissue image precisely [8]. In addition, Manitoba University has developed an

experimental device that collects observation data by moving up and down while mechanically rotating two wideband horns, and showed that it can detect foreign matter in the phantom even in the air interface between the phantom and the antenna [7]. However, clinical imaging with NFMI has not yet been reported.

In ST, which solves the inverse scattering problem, the complex permittivity distribution in the imaging region is reconstructed and the structure shape can be reproduced. However, the processing time is long because it is necessary to repeat the full-wave electromagnetic field analysis. In our research, even workstations with the latest GPUs take hours for a single analysis and days for image reconstruction. The biggest problem is that the phenomenon of radio wave propagation in the imaging region cannot be faithfully reproduced on a computer. It is extremely difficult to completely match the results of experiments with computer simulations that model microwave equipment with current numerical analysis technology for electromagnetic waves. The key to the realization of this technology is how to calibrate the experimental results and match them with the computer simulation. In this method, the breast is treated as a set of small hexahedrons or tetrahedra (called voxels), and the complex permittivity of each voxel is estimated. To improve the resolution is to make the voxels smaller, and the number of complex permittivity to be estimated increases on the order of the third power. In the inverse scattering problem, the governing equations are Born approximated and solved by replacing them with linear simultaneous equations, but this is an ill-posed problem with many unknowns (complex dielectric constant of each voxel) with respect to the number of equations. In this case, the reconstructed image looks like a defocused photograph because the sudden change in contrast between voxels cannot be reproduced. In addition, a highly sensitive antenna that can capture small changes in the complex permittivity of small voxels is required.

A group at Dartmath University has prototyped an imaging device with a structure in which 18 monopoles are submerged together with the breast in a matching fluid, and is performing clinical imaging [21]. The monopole array is moved up and down to acquire several observation data. For the imaging algorithm, forward analysis by Discrete Dipole Assumption (DDA) and inverse analysis by iterative method are adopted. Reconstructed images of scattered mammary glands accurately capture the location and size of the cancer, but the results of imaging the dense breast are not shown, and it seems that they have not reached the stage of practical use.

4. Imaging device

This section introduces the MI device and imaging results developed by the author. Only the equipment using CI was performed up to clinical imaging, but the equipment of ST and NFHI is in the stage of basic experiment.

4.1 CI for clinical test

4.1.1 System configuration

A schematic diagram and photographs of the developed microwave mammography equipment are shown in **Figure 7** [5]. The equipment comprised a sensor, an aspirator, an antenna switch, a network analyzer, a PC for control, and a workstation (WS) for data processing.

4.2.1 Printed dipole and FQCSA

4.2.1.1 Simulation model and method

Figure 10 shows the image sensor and phantom used in the computer simulation [25]. **Figure 10a** shows an imaging sensor in which two printed board dipoles arranged in an inverted L shape are inserted on the side of a dielectric block. **Figure 10b** shows an image sensor with a structure in which two FQSCAs arranged in an inverted L shape are pressed against the side surface of a dielectric block.

In this model, an imaging area of 40×40×40 mm is provided in the center of the dielectric block. The imaging area is modeled by cubic voxels with a side length of 10 mm or 5 mm. The number of voxels in the imaging area is 64 when the resolution is 10 mm and 512 when the resolution is 5 mm. In the image reconstruction using one frequency, the number of observation data is $_8C_2$ = 28, so it is an ill-posed problem with unknowns greater than the number of equations for any resolution. The distance between the imaging area and the antenna is 30 mm. The relative permittivity and conductivity of the dielectric block are 6.5 and 0.036 S/m.

Figure 11 shows photographs of the printed board dipole and FQSCA. The printed board dipole is mounted on a substrate with a thickness of 0.8 mm, relative dielectric constant of 3.8, and tanδ = 0.003. FQSCA is mounted on a substrate with a thickness of 1.6 mm, relative permittivity of 4, and tanδ = 0.011.

In order to evaluate image reconstruction quantitatively, the voxel number of the imaging area is determined as shown in **Figure 12**. As shown in **Figure 12**, the target of relative permittivity 39.6 and conductivity 1 S/m is set to 8 voxels in the center of the imaging area. The algorithm used for reconstruction is Distorted Born Iterative Method (DBIM) [14], the forward problem is solved with CST-Studio Suite [26], and the inverse problem is solved with MATLAB [27]. The frequency used for image reconstruction is 1.85 GHz for printed dipoles and 1.5 GHz for FQSCA. These are the frequencies of the lowest resonance point of each antenna.

4.2.1.2 Evaluation of image reconstruction

Figure 13 shows the results of reconstruction of the dielectric constant after 10 iterations assuming a resolution of 10 mm. Both the printed dipole and FQSCA show good reconstruction results. Note that the reconstruction result of the conductivity is omitted due to space limitations, but a reconstruction result equivalent to the relative dielectric constant has been confirmed.
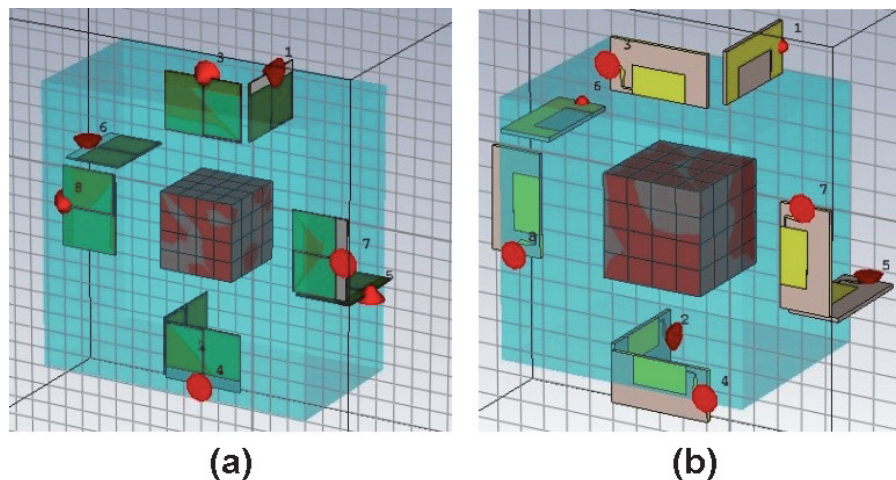

(a)   **(b)**

Figure 10.
(a) Simulated imaging sensor (printed dipole). (b) Simulated imaging sensor (FQSCA).

Figure 14 shows the results of reconstruction of the relative permittivity after 10 iterations, assuming a resolution of 5 mm, a relative permittivity of 39.6, and a conductivity of 1 S/m for only one voxel. Targets cannot be detected with printed dipoles, but targets can be detected with FQSCA.

4.2.2 Imaging sensor for clinical equipment

4.2.2.1 Design

Figure 15 shows the appearance of an imaging sensor for clinical trials using FQSCA and a breast modeled with hexahedral voxels. In this sensor, six FQSCA are arranged on the side of a 140×140×50 mm dielectric block, and 12 FQSCA are arranged on the upper surface with different polarization.

4.2.2.2 Simulation result

Figure 16a shows 3D distribution of permittivity and conductivity of the numerical breast phantom. **Figure 16b** shows the reconstructed 3D distribution of
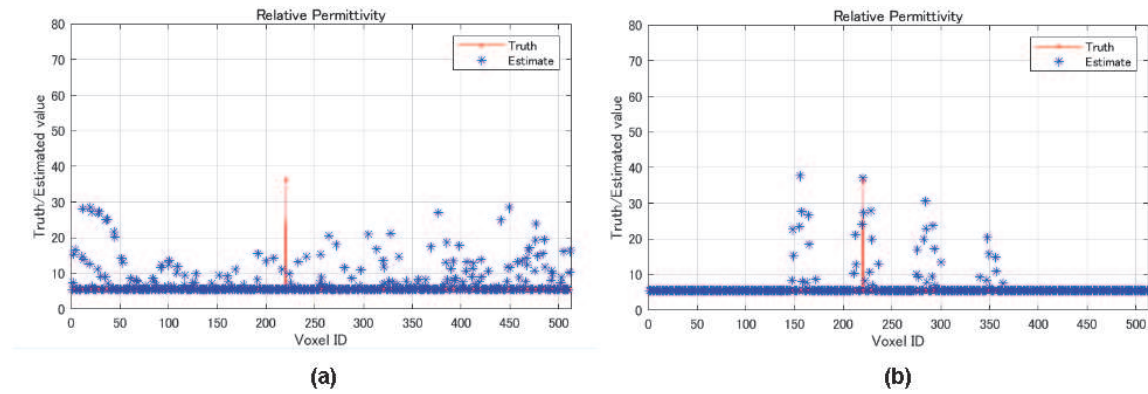
Figure 14.
(a) Reconstructed relative permittivity (resolution of 5 mm, printed dipole is used). (b) Reconstructed relative permittivity (resolution of 5 mm, FQSCA is used).
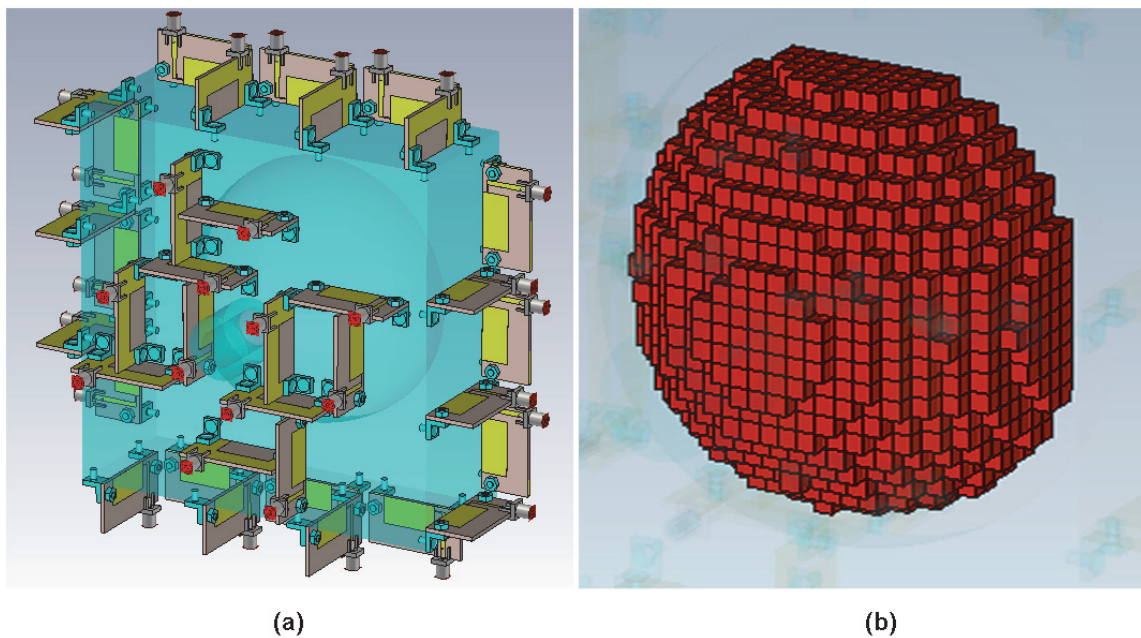
Figure 15.
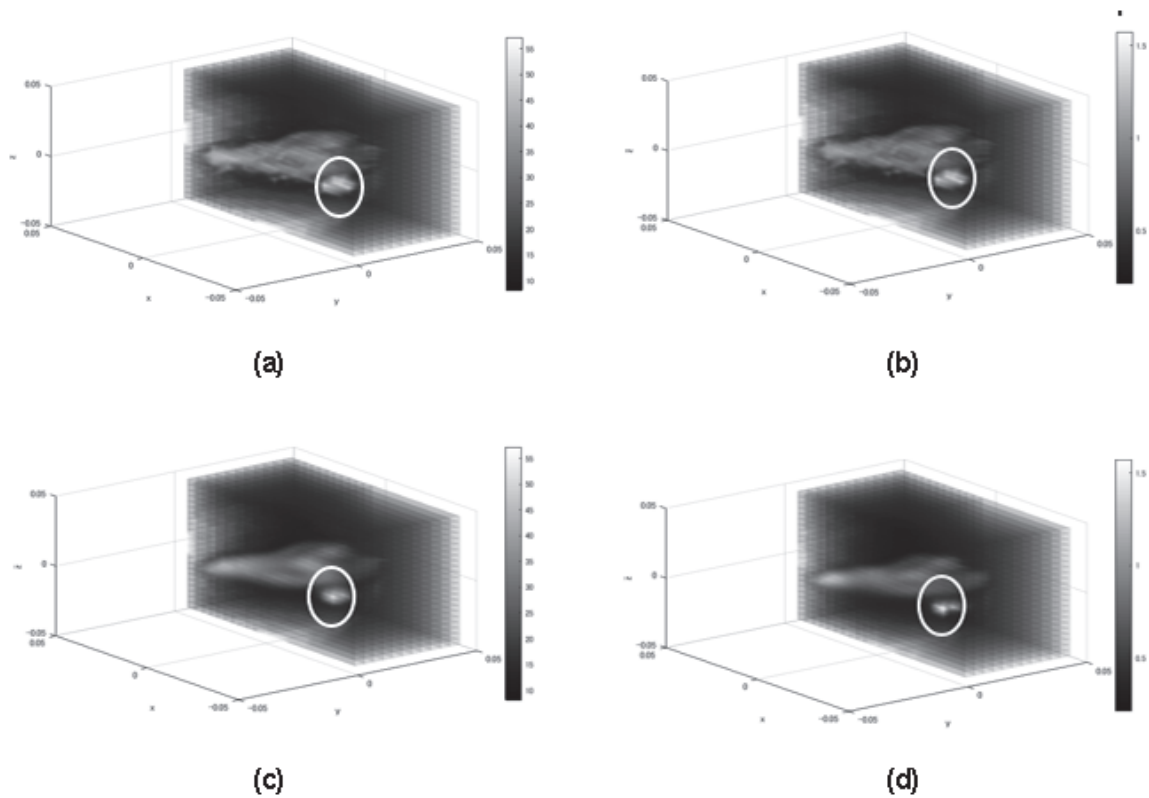*(a) Imaging sensor for clinical test. (b) Breast model.*

Figure 16.
(a) Set relative permittivity distribution. (b) Set conductivity. (c) Reconstructed relative permittivity distribution. (d) Reconstructed conductivity distribution.

permittivity and conductivity. The resolution is 4 mm and the frequency used is 1.5GHz. Circles indicate the cancer site. With the proposed sensor, mammary gland structure and cancer shape can be accurately reconstructed. The quality factor [28] evaluated by the complex dielectric constant was 0.96.

4.2.3 Manufacturing model

The sensor shown in **Figure 15** was prototyped and mounted on the system shown in **Figure 7**. **Figure 17** shows the prototype ST. The transmission characteristics of the antenna were measured with nothing in the cup that holds the breast, but as expected, they do not match the analysis results of CST Studio Suite. Therefore, we plan to adapt the measurement results to the simulation results by

Figure 17.
(a) Sensor for the manufacturing model. (b) Overview of the manufacturing model.

calibration based on the measurement of the reference object in [23], and proceed to clinical imaging.

4.3 NFHI

First, we confirm by computer simulation that NFHI can reconstruct intramammary tissue. Next, a simple image system is constructed and experimental verification is performed.

4.3.1 Simulation

Computer simulations were performed to confirm that NFHI can reconstruct intramammary tissue. **Figure 18** shows the simulation model, and **Table 5** shows the simulation conditions. Similar to X-ray mammography imaging, imaging is performed with a model in which the breast is sandwiched between two glass plates
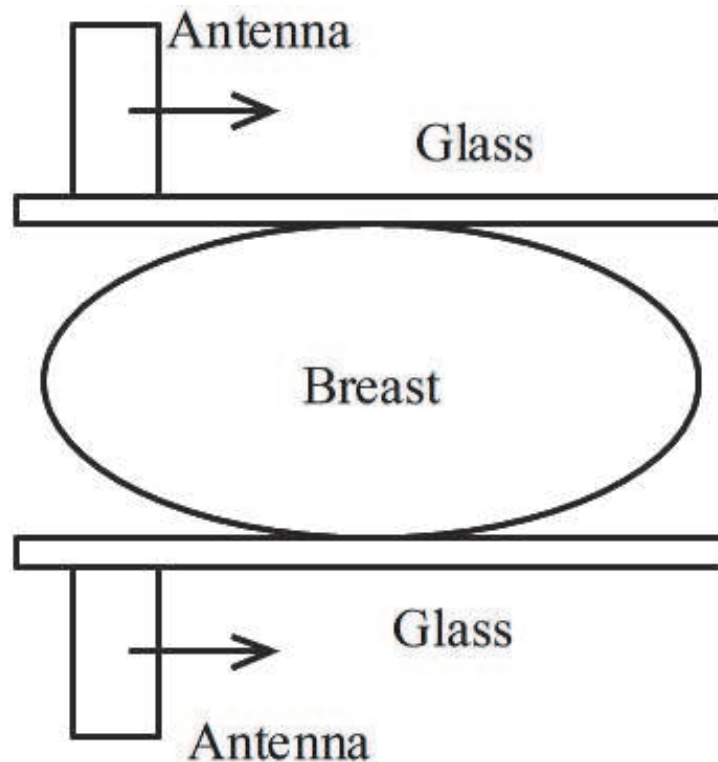
Figure 18.
Simulation model.

Frequency (GHz)		$20.4 \sim 26$
Scanning range (mm)	x-axis	$-50 \sim 50$
	y-axis	$0 \sim 50$
	z-axis	$-10 \sim 30$
Scanning step (mm)		2
CO	size(mm)	$2 \times 2 \times 2$
	permittivity	25
	Conductivity{S/m}	0.75

Table 5.
Simulation conditions.

and two antennas move on a plane at the same time. In order to obtain a resolution of 2 mm, the scattering parameters are acquired while the two antennas move in 2 mm steps on a plane of 100×50 mm. The frequency band used is 20.4-26GHz and the frequency step is 100 MHz. The antenna is a dipole antenna with a resonance frequency of 23.2 GHz. **Figure 19** shows the original tissue image and the reconstructed image. The reconstructed image faithfully reproduces the original image.

4.3.2 Measurement system

Figure 20 shows the appearance and system diagram of the imaging system used in the experiment. **Table 6** summarizes the measurement conditions.

The antennas are the commercially available primary feeds for Communication Satellite (CS) broadcast reception shown in **Figure 21**, and two antennas are arranged at intervals of 15 cm above and below, and can be scanned on the xy plane by an automatic stage. The imaging table is a celluloid plate with a thickness of 2 mm and 150×150 mm, and the height in the z-axis (vertical) direction can be adjusted by the z-axis stage. The outputs of the two CS antennas are connected to the input / output ports of the vector network analyzer, and the data of S_{11}, S_{21}, S_{12},
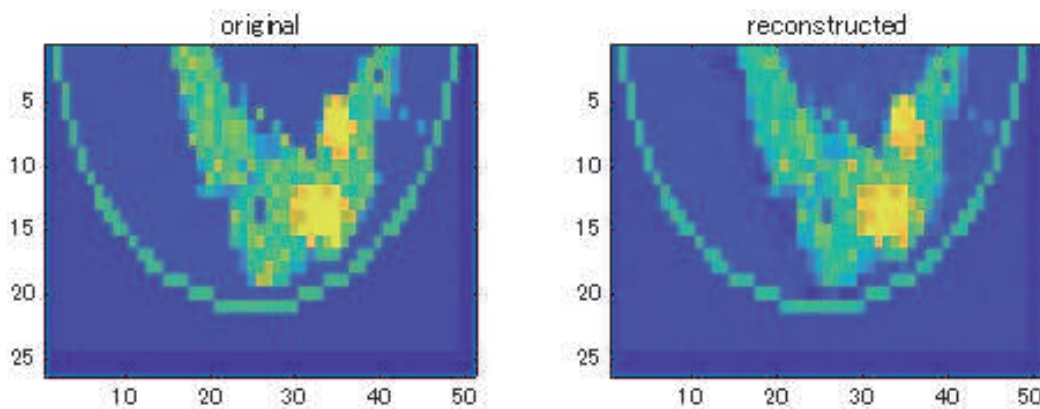

Figure 19.
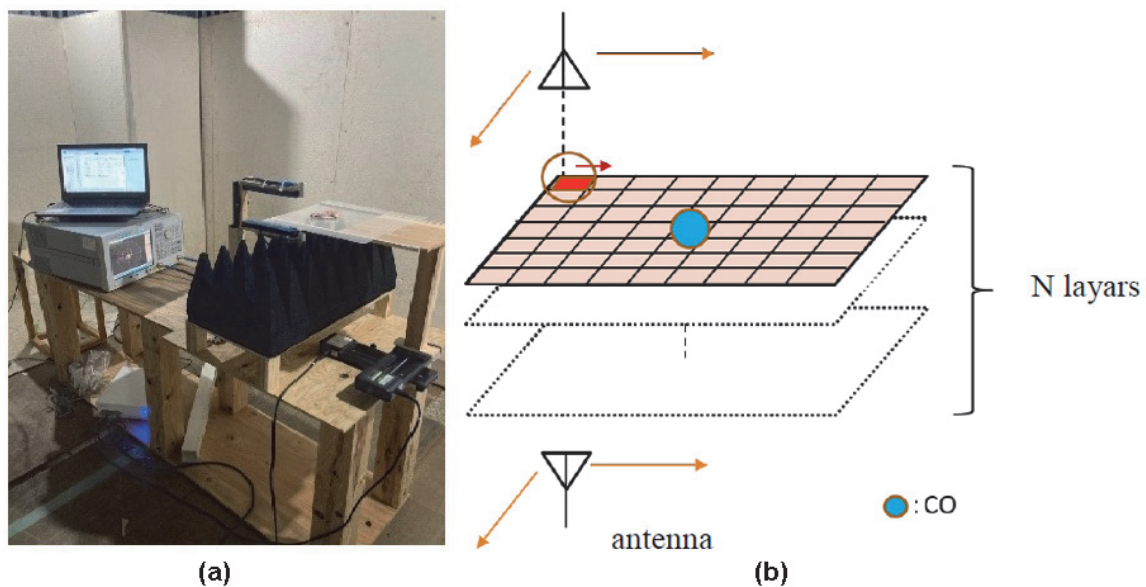*Original image (left) and reconstructed image (right).*

Figure 20.
(a) Overview of the NFHI system. (b) System configuration of NFHI system.

Frequency (GHz)		8.5 ~ 12.5
Scanning range (mm)	xy- plane	100 ~ 100
	z-axis	−10 ~ 30
Scanning step (mm)	xy-plane	2
	z-axis	10
CO(mm)		10 × 10 × 5

Table 6.
Measurement conditions.

Figure 21.
Feed antenna for communication satellites broadcast.

and S_{22} are measured while changing the relative positions of the antenna and the object. The calibration object (CO) is glycerin (relative permittivity: 4.042, dielectric loss tangent: 1.021 (10 GHz)) filled with a 10×10×5 mm ABS resin container in **Figure 20a**. The complex permittivity of glycerin was measured by the equipment described in Section 2.2.

4.3.3 Measurement

The CO was placed in the center of the imaging table, and the S-parameters of the CO were measured in 10 mm steps in the range of −10 mm to 30 mm on the z-axis. Next, the pork was placed on the imaging table at the position of z = 10 mm as shown in **Figure 22b**, and the S parameter was measured. In order to acquire the scattering component, the S-parameters of the background were measured at the positions of 10 mm steps of −10 mm to 30 mm on the z-axis, and this was subtracted from the S-parameters of the object. **Figure 23** shows a reconstructed image. It can be seen that the position and shape of the pork and the contrast between the lean and white meat are reproduced.

Bright spots may appear in the reconstructed image due to measurement error. This is because the measurement data on the xy plane has a measurement error corresponding to white noise. That is, when the white noise is inverse Fourier transformed, it becomes an impulse. In this case, the median filter used in image processing is effective. Take out a part of the measurement data (for example, 9×9 data) measured at the grid points every 2 mm on the xy plane, find the median value, and use this as the measurement result of the center position of the 9×9 data. This process eliminates the bright spots caused by noise and improves the quality of the reconstructed image.
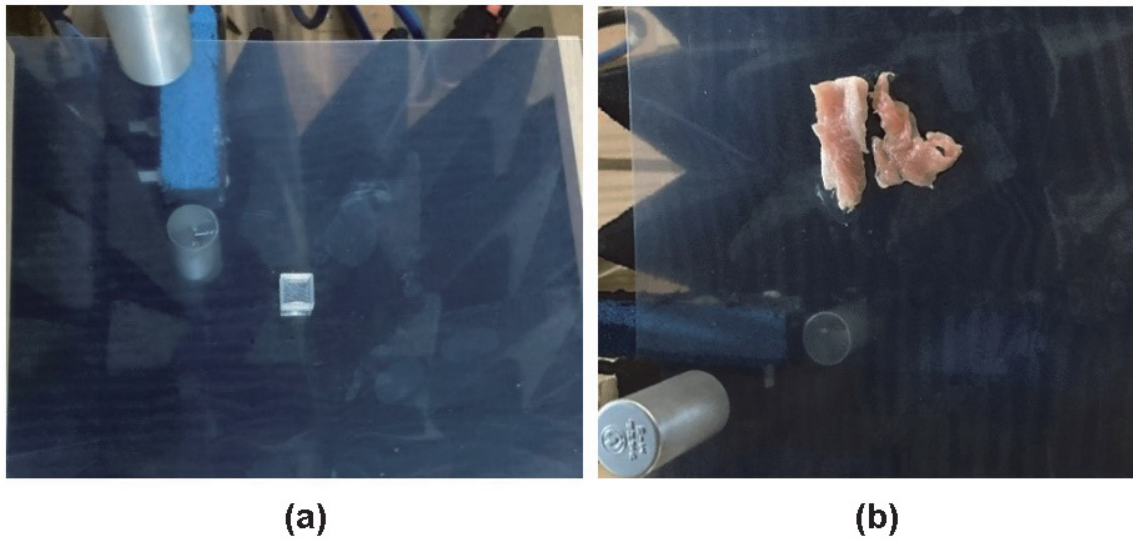
Figure 22.
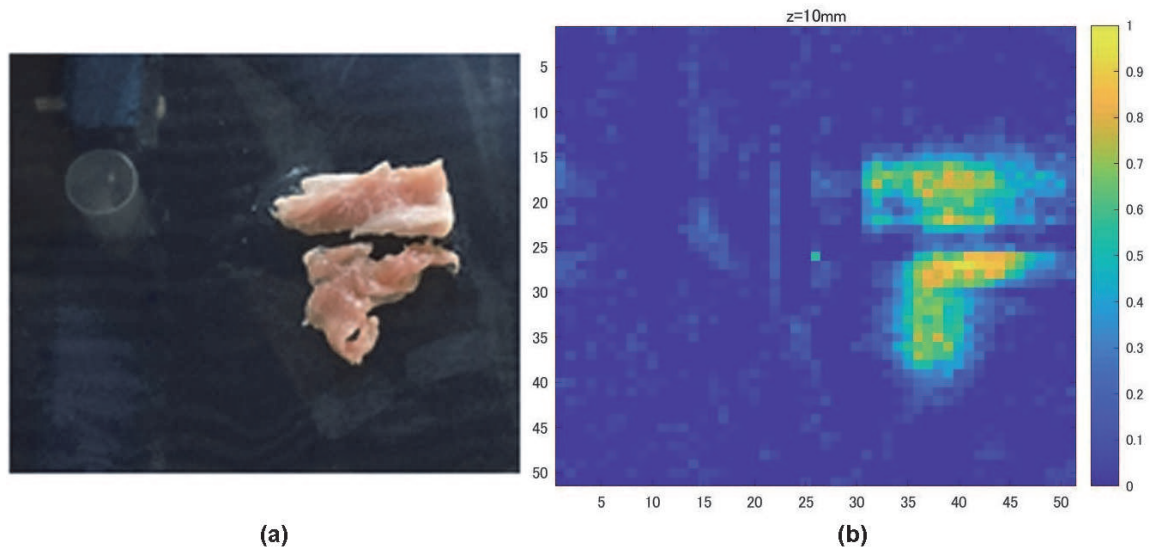*(a) Calibration object (CO) on the imaging table. (b) Pork placed on the imaging table.*

Figure 23.
(a) Original image. (b) Reconstructed image.

5. Conclusions

The breakthroughs required to put MI-based diagnostic imaging equipment into practical use are summarized below.

1. CI

How to extract only the scattered wave of the target (lesion) in the living body?

Reference [18] attempts to characterize breast cancer using all currently conceivable methods such as principal component analysis, independent component analysis, and kurtosis analysis. TR-MUSIC is applied to image reconstruction to improve the resolution. Clinical trial equipment has been developed and clinical trials have begun. In [19], the scattering response when the shape of the target (cancer) changes are analyzed and extraction of the

characteristics of the cancer is tried. In the future, it is thought that the development of technology to determine the presence or absence of cancer by giving a response signal to artificial intelligence will progress [29].

2. ST

Improvement of simulation technology: It is required to develop a numerical analysis method that matches the experiment and the simulation result, a sensor that has a structure that easily matches the simulation result, or to establish a calibration technology. It is also expected to speed up forward analysis using cloud computing and supercomputers.

3. NFHI

It is necessary to proceed with the development of high-density sensing technology to ensure the resolution, and to find a measure in which the Born approximation can be applied in the biometric environment.

Acknowledgements

Author details

Yoshihiko Kuwahara
Aichi Medical University, Nagakute, Japan

*Address all correspondence to: kuwahara.yoshihiko.296@mail.aichi-med-u.ac.jp

IntechOpen

[16] Hernandez-Lopez, M. A., Martin, R. G., A rotating array antennas for confocal microwave breast imaging, Microw. Opt. Technol. Lett., vol. 39(4), pp. 307-311, 2003.

[17] Bucci, O. M., Bellizi, G., Costanzo, S., Crocco, L., DI Massa, G., and Scapaticci, R., Assessing Detection Limits in Magnetic Nanoparticle Enhanced Microwave Imaging, IEEE Access vol.6, pp. 43192 – 43202, 2018.

[18] Fasoula, A., Duchesne, L., Gil Cano, J. D., Lawrence, P., Robin, G., and Bernard, J. G., On-Site Validation of a Microwave Breast Imaging System, before First Patient Study, diagnostic 2018, 8, 53, doi:10.3390.

[19] Davis, S. K., Van Veen, G. D., Hagness, S. C., and Kelcz, F., Breast Tumor Characterization Based on Ultrawideband Microwave Backscatter, IEEE Trans. on Biomedical Eng., Vol. 55 (1), pp.237-246, 2007.

[20] Amineh, R. K., Nikolova, N. K. and Ravan, M., Real Time Three Dimensional Imaging of Dielectric Bodies Using Microwave/Millimeter Wave Holography, ISBN 9781119538868, 2019.

[21] Grzegorczyk, T. M., Meaney, P. M., Kaufman, P. A., diFlorio-Alexander, R. M., and Paulsen, K. D., Fast 3D Tomographic Imaging for Breast Cancer Detection, IEEE trans. on Med. Imag. 31 (8), pp.1584-1592, 2012.

[22] Ono, Y. and Kuwahara, Y., Microwave Tomography Assisted by Radar Imaging, Proc. EUMC2017, 10.23919/EuMC.2017.8230985.

[23] Ostadrahimi, M., Mojabi, P., Gilmore, C., Zakaria, A., Noghanian, S., Pistorius, S., and LoVetri, J., Analysis of Incident Field Modeling and Incident/ Scattered Field Calibration Technique in Microwave Tomography, IEEE Antennas and Wireless Propagat. Lett., Vol.10, pp.900-903, 2011.

[24] Poretti, S., Lanini, M., Salvade, A., Maffongeli, M. and Monleone, R., Antenna Design for microwave Tomography Imaging of High Contrast Mediums, Proc. of EUCAP2017, pp.1708-1711, 2017.

[25] Kuwahara, Y. and Nozaki, A., Effectiveness of FQSCA to Microwave Imaging, Proc. of EUCAP, 10.23919/ EuCAP48036.2020.9136049.

[26] https://www.3ds.com/products-services/simulia/products/cst-studio-suite/

[27] https://jp.mathworks.com/discovery/what-is-matlab.html

[28] Shea, J. D., Van Veen, B. D., and Hagness, S. C., A TSVD Analysis of Microwave Inverse Scattering For Breast Imaging, IEEE Tran. on Biomed. Eng., Vol. 59(4) pp.936-945, 2012.

[29] Reimer, T, Sacristan, J. and Pistrius, S., Improving the Diagnostic Capability of Microwave Radar Imaging System Using Machine Learning, Proc. of EuCAP 2019, INSPEC Accession Number: 18775801.